Multi-Functionalized Polymers as Organic Cathodes for Sustainable Sodium/Potassium-Ion Batteries

Motahareh Mohammadiroudbari,[a] Kaiqiang Qin,[a] and Chao Luo*[a, b]

In this work, we designed and synthesized three novel polymeric cathode materials based on azo and carbonyl groups for Na-ion and K-ion batteries. The electrochemical performance of the polymer with a naphthalene backbone structure is better than that with benzene and biphenyl structures due to faster kinetics and lower solubility in the electrolyte. It unravels the rational design principle of extending π-conjugation aromatic structures in redox-active polymers to enhance the electrochemical performance. To further optimize the polymeric cathodes, the polymer with a naphthalene backbone structure is mixed with nitrogen-doped graphene to increase the conductivity and mitigate the dissolution. The resulting cathodes deliver high specific capacity, long cycle life, and fast-charging capability. Post-cycling characterizations were employed to study the chemical structure and morphology evolution upon cycling, demonstrating that the active centers (azo and carbonyl groups) in the polymer can undergo reversible redox reactions with Na^+/K^+ for sustainable alkali-ion batteries.

Introduction

After the launch in the 1990s, lithium-ion batteries (LIBs) dominate the energy storage market for portable electronics, electric vehicles, and grid-scale electrical energy storage.[1–3] Though state-of-the-art LIBs deliver high capacities and long cycle life, they cannot meet all the requirements for future applications such as carbon neutrality, high sustainability, and environmental benignity.[4–6] The ever-increasing demand for green, efficient and sustainable energy storage devices commenced a huge amount of research on the design of next-generation alkali-ion batteries.[7–11] It is desirable to find alternatives to lithium, where sodium and potassium with low cost, high abundance, and the most electrochemical similarity stand out.[12–16] To date, the cathodes used in Na-ion batteries (NIBs) and K-ion batteries (KIBs) are mostly based on inorganic materials, which suffer from low practical capacity, time- and energy-consuming synthetic processes, and structural instability upon long-term cycling. It impedes the efforts to reach net-zero carbon emission and long battery lifetime.[17] To address these challenges, transition metal-free organic cathode materials, consisting of lightweight atoms (e.g., C, H, O, and N) and flexible structures, offer opportunities for the development of high-performance, green and sustainable NIBs and KIBs.[18–21]

Due to high tunability and diverse nature, the capacity of organic cathode materials can be enhanced by introducing multiple redox-active centers into the chemical structure. Rational structural design of organic cathode materials provides promising candidates for high-performance NIBs and KIBs. However, small organic molecule-based cathode materials still encounter several challenges such as poor conductivity and high solubility in the electrolytes, which reduces the energy density and cycle life of organic batteries.[22,23] Polymerization is a promising approach to suppressing the solubility of small organic molecules in organic electrolytes. Redox-active polymers with flexible long chains offer fast reaction kinetics and rapid electron transfer.[24–27] Recently, polymers containing carbonyl functional groups were studied and showed promising electrochemical performance in LIBs and NIBs.[28–32] Among them, carbonyl-based polyimides have attracted considerable research interest owing to their high capacity, excellent mechanical strength, and favorable chemical resistance.[33–39] In addition, azo compounds as a category of organic electrode materials with excellent electrochemical performance in alkali-ion batteries also received extensive attention.[40,41] Therefore, design and synthesis of redox-active polymers containing both carbonyl and azo functional groups will be pivotal for the development and application of polymeric cathodes in NIBs and KIBs.

Herein, we designed three azo- and carbonyl-based polymers as cathodes in NIBs and KIBs for the first time. The polymers were synthesized through a one-pot condensation polymerization method under inert gas (Scheme S1). Three synthetic paths were taken using different dianhydride molecules to screen the best polymer as an active cathode material for NIBs and KIBs. Naphthalenetetracarboxylic dianhydride (NTCDA), pyromellitic dianhydride (PMDA), and 4,4'-biphthalic anhydride (BPDA) were reacted with 4,4'-azodianiline (ADA) for the polymer synthesis. The resulting multi-functionalized polymers are named as PNAI, PPAI, and PBAI. Their chemical
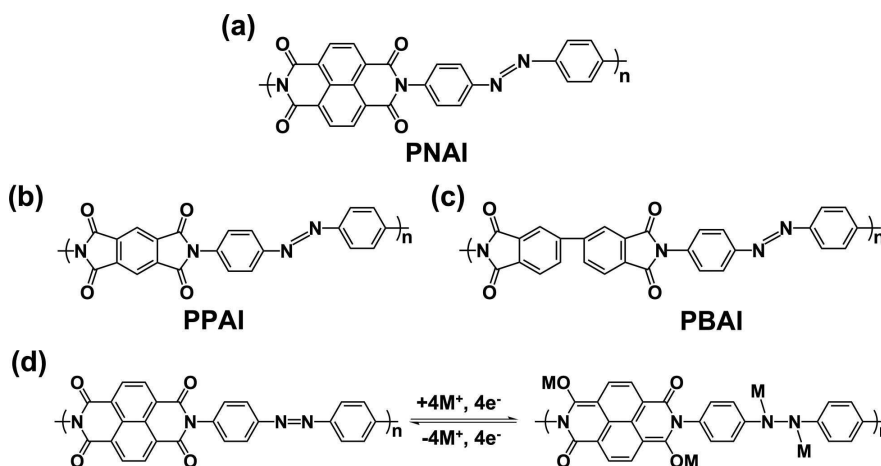
[a] M. Mohammadiroudbari, Dr. K. Qin, Prof. C. Luo
Department of Chemistry and Biochemistry
George Mason University
22030 Fairfax, VA, USA
E-mail: cluo@gmu.edu
[b] Prof. C. Luo
Quantum Science & Engineering Center
George Mason University
22030 Fairfax, VA, USA

Batteries & Supercaps

Research Article
doi.org/10.1002/batt.202200021

Chemistry Europe
European Chemical
Societies Publishing

Scheme 1. The molecular structure of three multi-functionalized polymers a) PNAI, b) PPAI, and c) PBAI; d) the proposed reaction mechanism, where M represents Na/K ion.

structures are shown in Scheme 1(a–c). The Fourier-transform infrared spectroscopy (FTIR) spectra of these polymers (Figure S1a) are similar due to the presence of the same functional groups. The scanning electron microscopy (SEM) images of PNAI (Figure 1d), PPAI (Figure S1b), and PBAI (Figure S1c) displayed the morphology of those polymers, indicating irregularly shaped microparticles for the three polymers. Among the three redox-active polymers, PNAI exhibited the best electrochemical performance in terms of high specific capacity, superior rate capability, and long cycle life. Therefore, PNAI was selected for further evaluating the electrochemical performance in NIBs and KIBs. In PNAI, the N≡N group provides two active sites to react with Na$^+$/K$^+$, while the four carbonyl groups can also participate in ion insertion/extraction. We propose that the redox reaction mechanism involves the azo group and two carbonyl groups from dianhydride in the PNAI (Scheme 1d). It could be difficult to access all four carbonyl groups during redox reactions because of the steric hindrance. The theoretical capacity for the polymer is calculated to be 241.45 mAh g^{-1} using the following equation:

$$C_{th} = n \times F/M,$$

where n is the number of ions, F is Faraday constant, and M is the molar mass of the repeating unit. To boost the conductivity and facilitate ion transfer in PNAI, nitrogen-doped graphene (NGR) was added to the polymeric cathode. The PNAI-NGR cathode can undergo a multi-electron redox reaction and deliver a high capacity and long cycle life in both NIBs and KIBs. Several characterization methods such as FTIR, Raman spectroscopy, SEM, and X-ray diffraction (XRD) were used to elucidate the structure and morphology of the PNAI-NGR composite. The fabricated coin cells with PNAI-NGR cathodes showed high capacities and excellent rate capability. The PNAI-NGR cathode delivered high reversible capacities of 206 mAh g^{-1} and 223 mAh g^{-1} at 50 mA g^{-1} in NIBs and KIBs, respectively. Further analysis revealed exceptional rate capability for both battery systems with reversible capacities of 167 mAh g^{-1} and 138 mAh g^{-1} at 1 A g^{-1} in NIBs and KIBs, respectively. The multiple redox sites in the repeating unit of the polymer combined with the highly conductive graphene framework facilitated ion diffusion despite the large size of Na and K ions.

Results and Discussion

The multi-functionalized polymer, PNAI, was synthesized using NTCDA and ADA according to a previously reported procedure (Scheme S1).[26] Multiple C≡O groups from NTCDA and the N≡N group from ADA are able to participate in sodiation/de-sodiation or potassiation/de-potassiation processes. PPAI and PBAI were synthesized via the same method. To confirm the polymerization reaction and investigate the morphology of polymeric samples, FTIR, XRD, Raman spectroscopy, elemental analysis, and SEM were performed. The dispersion of NGR in the composite sample was monitored by transmission electron microscopy (TEM). The fine powder of extracted polymer and NGR were characterized to explore the chemical structures.
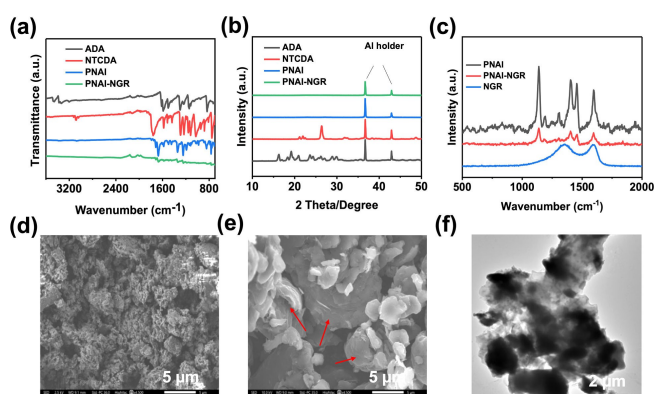

Figure 1. Material characterizations for the PNAI-NGR composite: a) FTIR spectra, b) XRD pattern, c) Raman spectra; d) SEM image of PNAI, e) SEM image of the PNAI-NGR composite with arrows pointed to the micro-sized graphene flakes, and f) TEM image of the PNAI-NGR composite.

Batteries & Supercaps

Research Article
doi.org/10.1002/batt.202200021

Chemistry
Europe
European Chemical
Societies Publishing

FTIR spectroscopy provides insight into the functional groups present in the structure of the polymer and the monomers. As shown in Figure 1(a), the stretching vibration of the $-NH_2$ bond in ADA (3300–3500 cm^{-1}) was disappeared in PNAI, indicating the successful reaction of amine groups with anhydride via a condensation polymerization.[26] The FTIR peaks for NTCDA related to the symmetric and asymmetric stretching vibrations of C=O at 1580 and 1760 cm^{-1} were preserved and slightly shifted to the lower wavenumbers due to the interaction of nitrogen atoms and two more aromatic rings in the repeating unit of PNAI.[27] The spectra for ADA and PNAI showed a pair of peaks between 1150 and 1350 cm^{-1}, representing the stretching vibration of the C–N bond in the monomer and the polymer.[26] The PNAI-NGR composite showed similar spectra to PNAI except for the intensity of the peaks, which was much lower due to the strong overlapping of PNAI and NGR. The FTIR spectra of PPAI and PBAI also showed the stretching vibration of C=O and disappearance of $-NH_2$ bond in ADA, confirming the success of the condensation polymerization. The crystalline structure of NTCDA and ADA was confirmed by the strong peaks between 15 and 30 degrees (Figure 1b), while there were no peaks recorded for PNAI and PNAI-NGR, verifying the amorphous structure of the polymer and random stacking of graphene layers. As shown in Figure 1(c), D-band and G-band for NGR can be observed in the range of 1300–1700 cm^{-1} in the Raman spectrum.[42] PNAI showed a Raman peak around 1100–1200 cm^{-1}, corresponding to the vibration of azo groups.[40] The peak at ~1600 cm^{-1} is related to cyclic ketone connected to nitrogen in the structure of the polymer.[43] The results for elemental analysis of PNAI, PPAI, and PBAI are provided in Table S1. In addition to the chemical structure, SEM images were also taken from PNAI, PPAI, PBAI, and PNAI-NGR powders to understand the morphology. The polymers displayed irregularly shaped micron-sized particles (Figures 1d, S1b and c), while the micron-sized graphene flakes were observed in Figure 1(e), showing good interaction with the polymeric particles. To further explore the morphology of the PNAI-NGR composite, TEM was used to confirm that NGR was fully dispersed in the composite. As shown in Figure 1(f), graphene layers could be found all over the surface of PNAI microparticles. More detailed TEM images for the PNAI-NGR composite are provided in Figure S2. These images demonstrated that NGR was capable to wrap polymeric microparticles and generate a uniform composite to enhance the conductivity of PNAI.

The electrochemical performances of PNAI, PPAI, and PBAI were evaluated by galvanostatic charge-discharge tests. The initial galvanostatic charge-discharge curves for PNAI, PPAI, and PBAI in NIBs are shown in Figure 2(a–c), where PNAI delivered higher redox potentials than PPAI and PBAI. The specific charge capacities of PBAI and PPAI are decreased very fast, whereas PNAI retained a high specific capacity for up to 100 cycles (Figure 2d). The chemical structure of three polymers varies due to the different types of dianhydrides used in the synthesis. In PNAI, the imide moiety in the repeating unit contains naphthalene, while the imide moieties in the repeating unit of PPAI and PBAI contain benzene and biphenyl, respectively.
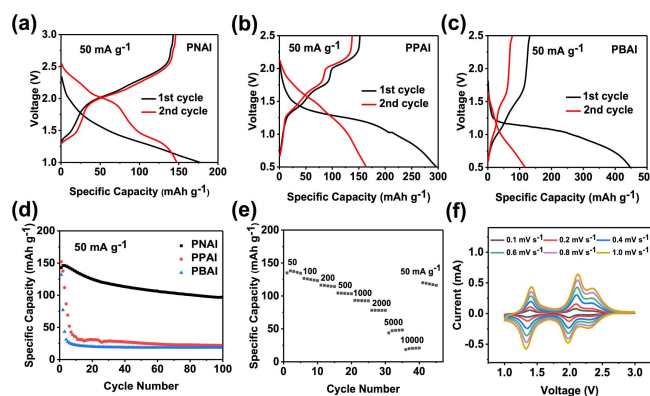

Figure 2. Galvanostatic charge-discharge curves in Na-ion batteries: a) PNAI, b) PPAI, c) PBAI; d) charge capacity at the current density of 50 mA g^{-1} for PNAI, PPAI, and PBAI; e) rate capability of PNAI at various current densities; f) cyclic voltammograms of PNAI at various scan rates.

Naphthalene has a larger aromatic structure than benzene and biphenyl, leading to better conductivity, lower solubility in the electrolyte, and higher stability upon repeated sodiation/desodiation processes. Our results indicate that extending π-conjugation aromatic structures in redox-active polymers is conducive for the electrochemical performance in NIBs. To exploit the reaction kinetics in NIBs, rate capability measurements, cyclic voltammetry (CV) at various scan rates, electrochemical impedance spectroscopy (EIS), and galvanostatic intermittent titration technique (GITT) were employed. As shown in Figure 2(e), the PNAI cathode showed good rate capability, but the capacities were lower than 150 mAh g^{-1} at 50 mA g^{-1}. The multi-electron redox mechanism was confirmed by the appearance of three pairs of sharp peaks in CV (Figure 2f), corresponding to the reversible reaction between carbonyl/azo groups and Na^+. The ex-situ Raman spectroscopy at different discharge and charge stages was performed to understand the reaction mechanism of the PNAI cathode in NIBs. As shown in Figure S3, the intensity of the peak at 1140 cm^{-1} decreases after discharging to 1.8 V, and a new peak at 1350 cm^{-1} appears, corresponding to sodiation of azo groups in PNAI.[40] The intensity of the peak at 1350 cm^{-1} increases, and the peak at 1140 cm^{-1} is disappeared after discharging to 1 V, demonstrating the full sodiation of the azo groups in PNAI. Meanwhile, the sharp peak at ~1600 cm^{-1} for carbonyl groups decreases due to the sodiation of carbonyl groups upon discharging. After recharging the PNAI cathode back to 3 V, the peak at 1140 cm^{-1} reappears, while the peak at 1350 cm^{-1} is disappeared, demonstrating the de-sodiation of azo groups. In addition, the sharp peak at ~1600 cm^{-1} is also recovered due to the de-sodiation of carbonyl groups upon charging. This result confirms the reversible redox reaction of azo groups and carbonyl groups in PNAI upon cycling. The pseudo-capacitive behavior of PNAI in NIBs was confirmed by slope values of natural logarithm of current versus scan rate, which are close to 1 (Figure S4a). In addition, the impedance test for the PNAI cathode in NIBs is shown in Figure S4(b). The Ohm resistance increases from ~15 ohm to ~75 ohm after 5 cycles, while the interfacial resistance represented by the

Batteries & Supercaps

Research Article
doi.org/10.1002/batt.202200021

Chemistry
Europe
European Chemical
Societies Publishing

depressed semi-circle dramatically decreases from ~450 ohm to ~150 ohm after 5 cycles. This may be due to the formation of stable solid electrolyte interphase between the PNAI cathode and the electrolyte after cycling.

Since PNAI shows the best performance among the three polymers, it is further mixed with NGR to optimize the performance of the polymeric cathode. The electrochemical performance of PNAI-NGR cathodes coupled with sodium metal was investigated in CR2032-type coin cells. The charge-discharge curves for the PNAI-NGR cathode in the cutoff window of 1–3 V are shown in Figure 3(a). The initial charge capacity of 206.2 mAh g^{-1} and discharge capacity of 255.4 mAh g^{-1} were achieved for the first cycle. Three pairs of redox plateaus centered at ~1.4 V, ~2.0 V, and ~2.3 V appeared in the second cycle, corresponding to anodic and cathodic peaks for the multi-electron reaction in the CV plot of the PNAI-NGR electrodes (Figure 3b). The long-term cyclic stability of PNAI-NGR cathodes was tested at different current densities of 50, 200, and 1000 mAh g^{-1}. The charge capacity decreased gradually upon cycling but remained stable for 200 cycles at 50 mA g^{-1} (Figure 3c). As shown in Figure 3(d), the charge capacity for the PNAI-NGR cathode is still retained at 129.5 mAh g^{-1} after 600 cycles at 200 mA g^{-1}. At a high current density of 1 A g^{-1}, the capacity is retained at above 100 mAh g^{-1} for 1,200 cycles, which is superior for an organic cathode in NIBs (Figure 3e). The stable cycling performance particularly at the high current density is promising for fast-charging batteries.
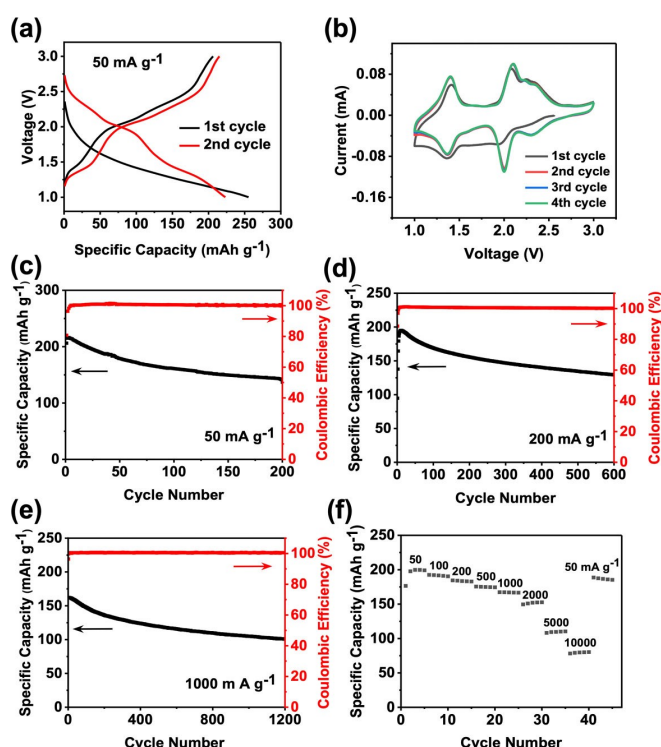
Moreover, all the cells demonstrated stable Coulombic efficiency of ~100% during long-term cycling. These results confirm the good cycling stability for PNAI-NGR cathodes in NIBs. To further evaluate the performance at various current densities, the rate capability test was conducted from 50 mA g^{-1} to 10 A g^{-1}. As shown in Figure 3(f), the reversible capacity of 110 mAh g^{-1} and 80 mAh g^{-1} were preserved at the high current density of 5 and 10 A g^{-1}. Additionally, the PNAI-NGR cathode recovered the reversible capacity of 187 mAh g^{-1} while returning to the starting current density, corresponding to a retention factor of 94%. These results for the PNAI-NGR cathode confirmed its high reversible capacity, robust reaction kinetics, and long cycle life in NIBs.

To further understand the fast kinetics of the redox reaction, CV at different scan rates, GITT, and EIS were performed on the polymer cathode. In CV, the PNAI-NGR cathode was cycled at the scan rates of 0.1–1 mV s^{-1} to track the intensity and shifting of the peaks (Figure 4a). The intensity of anodic and cathodic peaks enhanced with the elevated scan rates. As polarization increased at higher scan rates, cathodic and anodic peaks at ~2 V showed moderate shifting in potentials. As shown in Figure 4(b), the values for cathodic and anodic peaks were calculated to plot linear fit for the natural logarithm of current versus scan rates. The slopes, representing the b value ($I = a \times v^b$), are equal to 0.9625 and 0.9275 for anodic and cathodic peaks, respectively. These numbers are very close to 1, suggesting that the pseudo-capacitive behavior is dominant. The GITT test demonstrated low overpotential values (60/50 mV) for charge/discharge plateaus (Figure 4c). The charge/discharge equilibrium potentials are centered at 2 V correlating with the redox center previously recorded at first discharge-charge cycles. The results from CV and GITT verify the impressive rate capability of the PNAI-NGR cathode in NIBs. To analyze the dynamic changes occurring during charge-discharge cycles in the cell, EIS was employed. The depressed
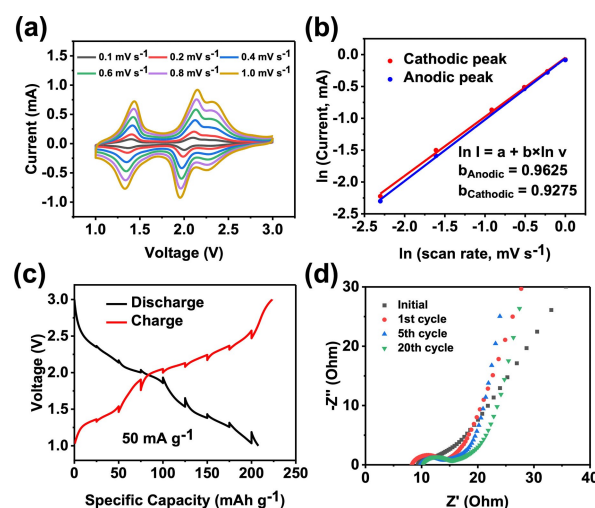

Figure 3. Electrochemical performance of PNAI-NGR in NIBs: a) g alvanostatic charge–discharge curves; b) cyclic voltammograms at 0.1 mV s^{-1}; de-sodiation capacity and Coulombic efficiency versus cycle number at the current density of c) 50 mA g^{-1}, d) 200 mA g^{-1}, e) 1,000 mA g^{-1}; f) rate capability at various current densities.

Figure 4. Reaction kinetics of PNAI-NGR in NIBs: a) cyclic voltammograms at various scan rates; b) the natural logarithm of peak current versus scan rate; c) potential response during GITT measurements; d) impedance analysis before and after cycling.

semi-circle and straight line in the Nyquist plot (Figure 4d) stand for the interfacial impedance and diffusion impedance. A low interfacial impedance of ~6 ohm was observed after the first cycle, and it was retained at ~10 ohm after 20 cycles, demonstrating the formation of a stable interphase layer on the polymer cathode. This is conducive to the long-term cycling stability of the PNAI-NGR cathode.

Since the PNAI-NGR cathodes exhibited superior performance in NIBs, we further evaluated their performance in KIBs using a similar ether-based electrolyte. Due to the universal nature of organic electrode materials in alkali-ion batteries, the excellent performance of the PNAI-NGR cathodes in NIBs was extended to KIBs. The galvanostatic discharge-charge curves demonstrated a charge capacity of 222.6 mAh g^{-1} and a discharge capacity of 269.0 mAh g^{-1} in the first cycle (Figure 5a). The charge capacity was retained in the second cycle,

and the cathode showed three charge plateaus at ~1.7 V, ~2.2 V, and ~2.7 V, corresponding to three discharge plateaus at ~1.6 V, ~2.1 V and ~2.5 V. To further exploit the charge-discharge behaviors, CV was conducted to check the anodic and cathodic peaks upon cycling. As shown in Figure 5(b), there are three pairs of sharp peaks centered at ~1.6 V, ~2.2 V, and ~2.5 V, confirming the multi-electron redox reaction. In the long-term cycling test (Figure 5c), the charge capacity at 50 mA g^{-1} remained above 200 mAh g^{-1} after 100 cycles. Even when cycling at a high current density of 500 mA g^{-1} (Figure 5d), the charge capacity of 153.1 mAh g^{-1} was still retained after 200 cycles, demonstrating a promising cycle life. The rate capability of the PNAI-NGR cathode was further assessed from 50 mA g^{-1} to 5 A g^{-1}. As shown in Figure 5(e), the PNAI-NGR cathode delivered an average charge capacity of 260 mAh g^{-1} at 50 mA g^{-1} and could retain a capacity above 50 mAh g^{-1} even at a high current density of 5 A g^{-1}. After the current density decreases back to 50 mA g^{-1}, the charge capacity of 268 mAh g^{-1} can be recovered immediately, demonstrating robust reaction kinetics in KIBs. To understand the kinetics, EIS and CV at various scan rates were carried out. As shown in Figure 5(f), the PNAI-NGR cathode was stabilized at a higher impedance of ~50 ohm after 20 cycles, in comparison to ~10 ohm in NIBs. It demonstrates slower reaction kinetics in KIBs than that in NIBs, which is consistent with the rate capability results in Figure 5(e). To further confirm it, the PNAI-NGR cathode was tested by CV at different scan rates (Figure 5g). The intensity of the peaks increased at higher scan rates. There was a similar shifting of cathodic peaks to lower potentials and anodic peaks to higher potentials. The linear fit for the natural logarithm of current versus scan rate was also plotted (Figure 5h). Similar to NIBs, the kinetics behavior is surface-controlled in KIBs as the calculated values for the slopes are very close to 1. Compared to the PNAI-NGR cathode, the PNAI cathode without NGR displayed different electrochemical behaviors. As shown in Figure S5(a), the PNAI cathode showed good rate capability, but the capacity is much lower than that of the PNAI-NGR cathode at the same current density due to the lower conductivity. The CV measurements at various scan rates were also performed (Figure S5b). The linear fit for the natural logarithm of current versus scan rate showed the reaction kinetics is controlled by the diffusion behavior (Figure S5c) since the slope values are close to 0.5. The pseudo-capacitive behavior of the PNAI cathode in NIBs but the diffusion-controlled behavior in KIBs is due to the larger ion size of K$^+$ than Na$^+$. The large ion size induces a large hindrance and limits the diffusion of K$^+$ in the PNAI cathode, resulting in worse reaction kinetics in KIBs than that in NIBs. NGR can accelerate ion diffusion in the cathode, leading to fast reaction kinetics with a pseudo-capacitive behavior as the dominant mechanism. The effect of NGR on the cycling performance of PNAI is presented in Figure S6 for NIBs and KIBs, confirming the higher capacity and better cycle life for the cathodes with NGR. As controls, NGR electrodes without PNAI were also assessed in NIBs and KIBs. The charge-discharge curves did not show any plateaus (Figure S7). The reversible capacity of NGR electrodes are ~25 mAh g^{-1} and ~80 mAh g^{-1}
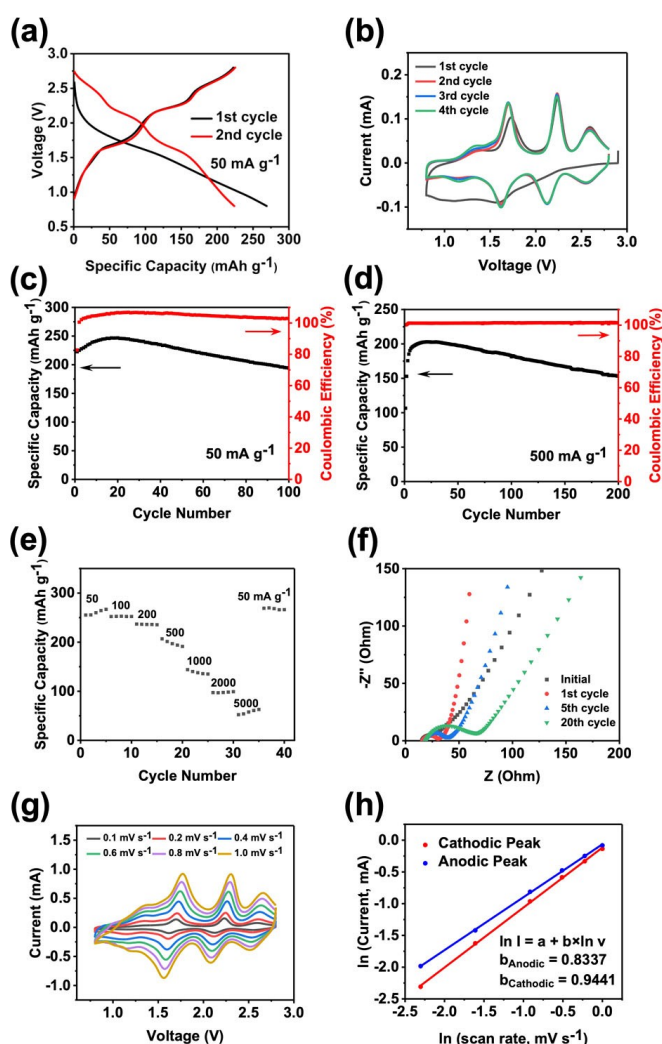

Figure 5. Electrochemical performance of the PNAI-NGR cathode in KIBs: a) galvanostatic charge-discharge curves; b) cyclic voltammograms at 0.1 mV s^{-1}; de-potassiation capacity and Coulombic efficiency versus cycle number at the current density of c) 50 mA g^{-1} and d) 500 mA g^{-1}; e) rate capability at various current densities; f) impedance analysis before and after cycling; g) cyclic voltammograms at various scan rates; h) the natural logarithm of peak current versus scan rate.

Batteries & Supercaps

Research Article
doi.org/10.1002/batt.202200021

Chemistry Europe
European Chemical
Societies Publishing

at 50 mA g^{-1} in NIBs and KIBs, respectively, demonstrating limited capacity contribution from NGR in the PNAI-NGR cathodes. The specific capacity in Figure 5 is calculated based on the weight of PNAI in the cathode. Since the capacity of NGR in KIBs (∼80 mAh g^{-1} at 50 mA g^{-1}) is much higher than that in NIBs (∼25 mAh g^{-1} at 50 mA g^{-1}) as shown in Figure S7, the specific capacity of the PNAI-NGR cathode is also calculated based on the total weight of PNAI and NGR. Figure S8 shows the electrochemical performance of the PNAI-NGR cathode in KIBs based on the total weight of PNAI and NGR.

To understand the reason behind the excellent performance, XRD, FTIR, and SEM were used to study the structure evolution of the cathodes in NIBs and KIBs. As shown in Figure 6(a), the FTIR spectra did not show any change for the PNAI cathodes in NIBs from the pristine electrode to the 20th cycle, demonstrating no chemical structural change upon cycling. The SEM images before cycling and after 1st and 20th cycle (Figure 6c) did not show any morphological destruction of the PNAI cathode in NIBs. Analogous to the PNAI cathodes,

the PNAI-NGR cathodes also maintained the morphological structure upon cycling (Figure 6d). The polymeric particles maintained the irregular shapes with random dispersion of graphene layers. As shown in Figure 6b, the identical FTIR peaks for PNAI are also preserved in KIBs after 20 cycles. Comparing SEM images of the PNAI cathodes and the PNAI-NGR cathodes before cycling and after 1st and 20th cycle in KIBs (Figure 6e and 6f), no morphological change can be observed, demonstrating that the flexible PNAI polymer and NGR can withstand the large volume change caused by K-ion insertion and extraction during the repeated charge/discharge cycles. The XRD pattern (Figure S9) of the PNAI cathodes did not exhibit any peaks since the PNAI polymer maintained its amorphous structure upon cycling. These results confirm the stable chemical and morphological structure of PNAI and PNAI-NGR in NIBs and KIBs upon cycling, which contributes to the superior electrochemical performance.

Conclusion

In summary, multi-functionalized polymers (PNAI, PPAI, and PBAI) based on carbonyl and azo groups were designed and synthesized as organic cathode materials for NIBs and KIBs. Among the three redox-active polymers, the PNAI cathode showed the best electrochemical performance in NIBs and KIBs, offering multi-electron redox reactions with Na$^+$/K$^+$. This result demonstrates that the naphthalene structure is better than the benzene and biphenyl structures in the redox-active polymers to enhance the conductivity and reduce the solubility in the electrolyte. Hence, the rational design of extended π-conjugation structures in redox-active polymers could improve the electrochemical performance in NIBs and KIBs. To further enhance the battery performance, the PNAI-NGR composite was prepared as a cathode material, which delivered high capacities and rate capability in NIBs and KIBs. Taking advantage of two types of redox centers (N═N and C═O) and highly conductive NGR, reversible ion insertion/extraction occurred even at high current densities up to 10 A g^{-1}. The fast reaction kinetics was confirmed by CV, EIS, and GITT. Several characterization methods were used to track structural and morphological changes during cycling, confirming a robust structure for the PNAI-NGR cathode. Therefore, this work demonstrates that the multi-functionalized polymer containing both azo and carbonyl functional groups exhibits high performance in NIBs and KIBs, offering great opportunities to develop high-performance, green, and sustainable batteries.

Figure 6. Electrode characterizations before and after cycling: a) FTIR spectra of the pristine and cycled PNAI cathodes in NIBs; b) FTIR spectra of the pristine and cycled PNAI cathodes in KIBs; c) SEM images of the pristine and cycled PNAI cathodes in NIBs; d) SEM images of the pristine and cycled PNAI-NGR cathodes in NIBs; e) SEM images of the pristine and cycled PNAI cathodes in KIBs; f) SEM images of the pristine and cycled PNAI-NGR cathodes in KIBs.

Experimental Section

Materials

Naphthalenetetracarboxylic dianhydride (>97%) and 4,4'-Azodianiline (95%) were purchased from TCI and ACROS organics respectively, and they were used as received. Dimethylformamide (99.8%) was purchased from Sigma-Aldrich and stirred for 24 h with magnesium sulfate to remove any trace of water before using
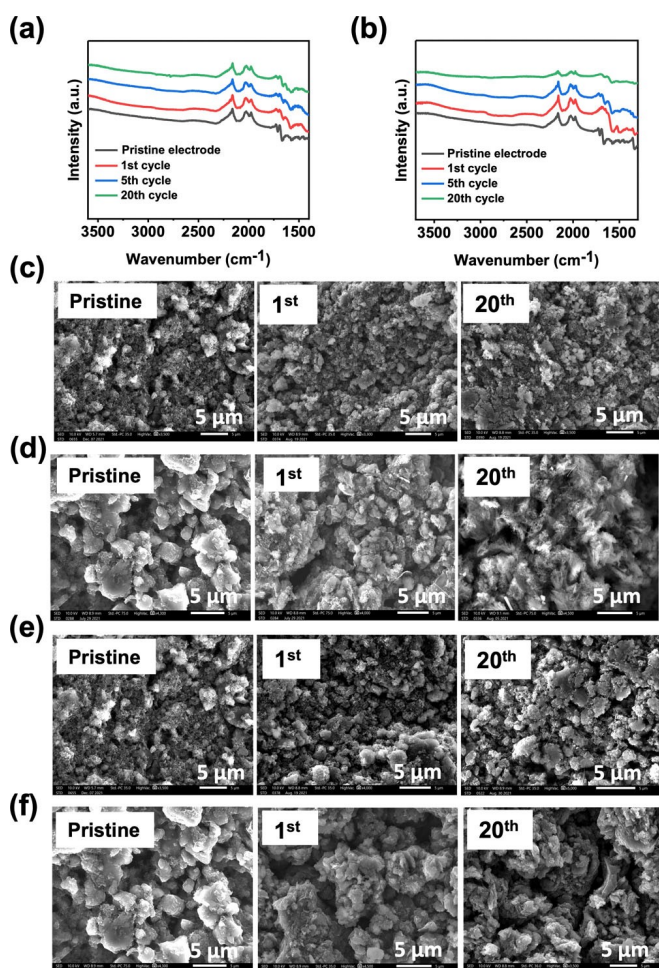
Batteries & Supercaps

Research Article
doi.org/10.1002/batt.202200021

Chemistry Europe
European Chemical
Societies Publishing

it for synthesis. The Nitrogen-doped single-layer graphene was received from ACS materials and carbon black (Super P) with above 99% purity was purchased from Alfa Aesar. The binder solution was prepared using sodium alginate purchased from MP Biomedicals. Electrolyte components including diethylene glycol dimethyl ether (>99%) and sodium hexafluorophosphate (>99%) were purchased from TCI and Alfa Aesar, respectively.

Synthesis of the polymers

The PNAI polymer was synthesized following the procedure reported by Tian et al.[26] Naphthalenetetracarboxylic dianhydride (NTCDA) was dissolved in 30 mL of Dimethylformamide (DMF) in a 100 mL three-necked flask under refluxing and degassing. 4,4'-Azodianiline was dissolved in 10 mL of DMF and added to the solution stirring at 140°C under Nitrogen gas and stirring continued under N_2 atmosphere for 3 days. The obtained amber-colored precipitation was collected by centrifuge and washed with methanol and acetone 3 times, respectively. The resulting solid was dried at 80°C in a vacuum oven overnight. PPAI and PBAI were synthesized using the same method.

Characterization

X-ray diffraction (XRD) pattern was performed by Rigaku MiniFlex using CuKα radiation; Fourier-transform infrared spectroscopy (FTIR) was recorded by Agilent Cary 630 FTIR Spectrometer; Raman spectra were taken by Horiba XploRA PLUS Raman microscope; scanning electron microscopy (SEM) images were taken by JEOL JSM-IT500HR, and transmission electron microscopy (TEM) images were taken by JEOL 1400F.

Electrochemical measurements

The polymeric cathodes were fabricated using PNAI/PPAI/PBAI, carbon black (CB), and sodium alginate (SA) in the ratio of 6:3:1 to form a smooth slurry. The electrodes were prepared by casting the slurry onto aluminum foil using a doctor blade and dried in a vacuum oven at 80°C overnight. The dried film was punched into circular electrodes with an average mass loading of 2.0 mg cm^{-2}. The PNAI powder was ground with graphene (the ratio of 2 to 1) for about one hour to make a homogenous mixture. Subsequently, CB and SA were added to form a slurry at the weight ratio of 8:1:1 resulting in electrodes with an average mass loading of 2.2 mg cm^{-2}. The coin cells for Na-ion half cells were assembled using sodium metal as the counter electrode, 2 M NaPF$_6$ in ethylene glycol dimethyl ether (DEGDME) as the electrolytes, and glass fiber (Whatman) as the separator. The K-ion cells were assembled using potassium metal as the counter electrode, 2.8 M KPF$_6$ in DEGDME, and glass fiber as the separator. The electrochemical performance was tested using an Arbin battery test station. Cyclic voltammograms (CVs) were recorded by Gamry Reference 1010E Potentiostat/Galvanostat/ZRA with a scan rate of 0.1–1.0 mV s^{-1}. Impedance analysis was also performed by Gamry Reference 1010E Potentiostat/Galvanostat/ZRA.

To conduct the FTIR test before and after cycling, coin cells with PNAI as the cathode and sodium metal as the counter electrode were assembled. The cells were disassembled in the glovebox after cycling at 50 mA g^{-1} for 1, 5, and 20 cycles. The cycled electrodes were washed by DEGDME and dried in a vacuum oven at 80°C overnight. Afterward, the pristine and cycled electrodes were characterized by Agilent Cary 630 FTIR Spectrometer. For XRD tests before and after cycling, high mass loading electrodes were fabricated using polytetrafluoroethylene (PTFE) as a binder to improve the strength of the XRD signal. PNAI, CB, and PTFE were mixed in the ratio of 6:3:1 to get a smooth film. The thick electrodes were tested at the same condition mentioned above, after drying in a vacuum oven at 80°C overnight.

Conflict of Interest

The authors declare no conflict of interest.

Data Availability Statement

The data that support the findings of this study are available from the corresponding author upon reasonable request.

[1] M. Li, J. Lu, Z. Chen, K. Amine, *Adv. Mater.* **2018**, *30*, 1800561.
[2] Z. P. Cano, D. Banham, S. Ye, A. Hintennach, J. Lu, M. Fowler, Z. Chen, *Nat. Energy* **2018**, *3*, 279.
[3] J. B. Goodenough, K. S. Park, *J. Am. Chem. Soc.* **2013**, *135*, 1167.
[4] Y. He, B. Matthews, J. Wang, L. Song, X. Wang, G. Wu, *J. Mater. Chem. A* **2018**, *6*, 735.
[5] K. Qin, K. Holguin, M. Mohammadiroudbari, J. Huang, E. Y. S. Kim, R. Hall, C. Luo, *Adv. Funct. Mater.* **2021**, *31*, 2009694.
[6] M. Huang, M. Li, C. Niu, Q. Li, L. Mai, *Adv. Funct. Mater.* **2019**, *29*, 1807847.
[7] S. A. Khan, S. Ali, K. Saeed, M. Usman, I. Khan, *J. Mater. Chem. A* **2019**, *7*, 10159.
[8] S. S. Zhang, *ChemElectroChem* **2020**, *7*, 3569.
[9] Z. Wu, D. Adekoya, X. Huang, M. J. Kiefel, J. Xie, W. Xu, Q. Zhang, D. Zhu, S. Zhang, *ACS Nano* **2020**, *14*, 12016.
[10] Z. Wu, J. Xie, Z. J. Xu, S. Zhang, Q. Zhang, *J. Mater. Chem. A* **2019**, *7*, 4259.
[11] C. Peng, G. H. Ning, J. Su, G. Zhong, W. Tang, B. Tian, C. Su, Di. Yu, L. Zu, J. Yang, M. F. Ng, Y. S. Hu, Y. Yang, M. Armand, K. P. Loh, *Nat. Energy* **2017**, *2*, 17074.
[12] P. K. Nayak, L. Yang, W. Brehm, P. Adelhelm, *Angew. Chem. Int. Ed.* **2018**, *57*, 102.
[13] R. Rajagopalan, Y. Tang, C. Jia, X. Ji, H. Wang, *Energy Environ. Sci.* **2020**, *13*, 1568.
[14] K. Holguin, M. Mohammadiroudbari, K. Qin, C. Luo, *J. Mater. Chem. A* **2021**, *9*, 19083.
[15] W. Zhang, Y. Liu, Z. Guo, *Sci. Adv.* **2019**, *5*, eaav7412.
[16] K. Qin, J. Huang, K. Holguin, C. Luo, *Energy Environ. Sci.* **2020**, *13*, 3950.
[17] C. Niu, J. Meng, X. Wang, C. Han, M. Yan, K. Zhao, X. Xu, W. Ren, Y. Zhao, L. Xu, Q. Zhang, D. Zhao, L. Mai, *Nat. Commun.* **2015**, *6*, 7402.
[18] Y. Chen, W. Luo, M. Carter, L. Zhou, J. Dai, K. Fu, S. Lacey, T. Li, J. Wan, X. Han, Y. Bao, L. Hu, *Nano Energy* **2015**, *18*, 205.
[19] B. Esser, F. Dolhem, M. Becuwe, P. Poizot, A. Vlad, D. Brandell, *J. Power Sources* **2021**, *482*, 228814.
[20] Y. Xu, M. Zhou, Y. Lei, *Mater. Today* **2018**, *21*, 60.

[21] G. Dai, Y. Liu, Z. Niu, P. He, Y. Zhao, X. Zhang, H. Zhou, *Matter* **2019**, *1*, 945.

[22] J. Xie, P. Gu, Q. Zhang, *ACS Energy Lett.* **2017**, *2*, 1985.

[23] Y. Hu, H. Ding, Y. Bai, Z. Liu, S. Chen, Y. Wu, X. Yu, L. Fan, B. Lu, *ACS Appl. Mater. Interfaces* **2019**, *11*, 42078.

[24] S. Muench, A. Wild, C. Friebe, B. Häupler, T. Janoschka, U. S. Schubert, *Chem. Rev.* **2016**, *116*, 9438.

[25] J. Yang, Y. Shi, P. Sun, P. Xiong, Y. Xu, *ACS Appl. Mater. Interfaces* **2019**, *11*, 42305.

[26] B. Tian, J. Zheng, C. Zhao, C. Liu, C. Su, W. Tang, X. Li, G. H. Ning, *J. Mater. Chem. A* **2019**, *7*, 9997.

[27] J. Li, M. Luo, Z. Ba, Z. Wang, L. Chen, Y. Li, M. Li, H. B. Li, J. Dong, X. Zhao, Q. Zhang, *J. Mater. Chem. A* **2019**, *7*, 19112.

[28] J. Xie, Z. Wang, Z. J. Xu, Q. Zhang, *Adv. Energy Mater.* **2018**, *8*, 1703509.

[29] L. Zhu, G. Ding, L. Xie, X. Cao, J. Liu, X. Lei, J. Ma, *Chem. Mater.* **2019**, *31*, 8582.

[30] Q. Li, D. Li, H. Wang, H. G. Wang, Y. Li, Z. Si, Q. Duan, *ACS Appl. Mater. Interfaces* **2019**, *11*, 28801.

[31] C. Zhang, Y. Qiao, P. Xiong, W. Ma, P. Bai, X. Wang, Q. Li, J. Zhao, Y. Xu, Y. Chen, J. H. Zeng, F. Wang, Y. Xu, J. X. Jiang, *ACS Nano* **2019**, *13*, 745.

[32] A. Molina, N. Patil, E. Ventosa, M. Liras, J. Palma, R. Marcilla, *ACS Energy Lett.* **2020**, *5*, 2945.

[33] G. Hernández, N. Casado, A. M. Zamarayeva, J. K. Duey, M. Armand, A. C. Arias, D. Mecerreyes, *ACS Appl. Energ. Mater.* **2018**, *1*, 7199.

[34] H. Banda, D. Damien, K. Nagarajan, M. Hariharan, M. M. Shaijumon, *J. Mater. Chem. A* **2015**, *3*, 10453.

[35] Z. Ba, Z. Wang, M. Luo, H. B. Li, Y. Li, T. Huang, J. Dong, Q. Zhang, X. Zhao, *ACS Appl. Mater. Interfaces* **2020**, *12*, 807.

[36] M. R. Raj, N. Kim, G. Lee, *Sustain. Energy Fuels* **2021**, *5*, 175.

[37] M. Ruby Raj, R. V. Mangalaraja, D. Contreras, K. Varaprasad, M. V. Reddy, S. Adams, *ACS Appl. Energ. Mater.* **2020**, *3*, 240.

[38] Y. Huang, K. Li, J. Liu, X. Zhong, X. Duan, I. Shakir, Y. Xu, *J. Mater. Chem. A* **2017**, *5*, 2710.

[39] X. C. Tu, Z. Wu, X. Geng, L. L. Qu, H. M. Sun, C. Lai, D. S. Li, S. Zhang, *J. Mater. Chem. A* **2021**, *9*, 18306.

[40] C. Luo, O. Borodin, X. Ji, S. Hou, K. J. Gaskell, X. Fan, J. Chen, T. Deng, R. Wang, J. Jiang, C. Wang, *Proc. Natl. Acad. Sci. USA* **2018**, *115*, 2004.

[41] C. Luo, G. L. Xu, X. Ji, S. Hou, L. Chen, F. Wang, J. Jiang, Z. Chen, Y. Ren, K. Amine, C. Wang, *Angew. Chem. Int. Ed.* **2018**, *57*, 2879.

[42] H. Kim, K. Y. Park, J. Hong, K. Kang, *Sci. Rep.* **2014**, *4*, 1.

[43] M. Ruby Raj, R. V. Mangalaraja, D. Contreras, K. Varaprasad, M. V. Reddy, S. Adams, *ACS Appl. Energ. Mater.* **2020**, *3*, 240.